PAPER

Quantum neural network-inspired variational quantum circuit for simulating diamond ^{14}NV center Hamiltonian with a proximal ^{13}C isotope

To cite this article: Chisomo Daka and Somnath Bhattacharyya 2025 *Phys. Scr.* **100** 025111

Physica Scripta

PAPER

Quantum neural network-inspired variational quantum circuit for simulating diamond ^{14}NV center Hamiltonian with a proximal ^{13}C isotope

RECEIVED
30 August 2024

REVISED
12 November 2024

ACCEPTED FOR PUBLICATION
3 January 2025

PUBLISHED
17 January 2025

Chisomo Daka and Somnath Bhattacharyya

Nano-Scale Transport Physics Laboratory, School of Physics, University of the Witwatersrand, Johannesburg, 1 Jan Smuts Avenue, Wits 2050, South Africa

E-mail: somnath.bhattacharyya@wits.ac.za

Keywords: NV center, variational quantum circuit, quantum neural network, qubits

Abstract

We present a variational quantum circuit (VQC) that utilizes the architecture of a quantum neural network (QNN) to simulate hyperfine interactions in diamond nitrogen vacancy (NV) centers, which is typically a challenging task for traditional computation methods. Isotopes of ^{13}C, though naturally rare, possess a nuclear spin ($l = \frac{1}{2}$) which anisotropically interacts with the NV center's electron spin, resulting in distinct hyperfine structure and coherence properties. The VQC's ansatz unitary was implemented stepwise (through optimization *Trotter* steps) to mimic a multi-layered QNN configuration. The dynamical evolution of the ^{14}NV-^{13}C Hamiltonian was simulated while maintaining flexibility for optimization on noisy intermediate-scale quantum (NISQ) platforms. Qiskit SDK was used to design and execute the circuit on 127-qubit IBM quantum hardware. Ansatz parameters were optimized using six classical optimization algorithms initialized with pseudo-random parameter vectors. We successfully determined optimal ansatz parameters for estimating the minimum energy eigenvalues of the ^{14}NV-^{13}C observable using the VQC's cost function, enabling us to model the system's ground state dynamics. Our findings show that gradient-free optimizers are efficient for the designed *Hardware Efficient SU(2) 2-local circuit* (ESU2) ansatz, characterized by a barren plateau landscape. We further established that a maximally entangled VQC initialization (i.e., GHZ_3) retains its entanglement scheme irrespective of the optimization pathway. Hence, this approach highlights the effectiveness of QNN-inspired VQC circuits for accurately simulating NV centers coupled with strongly interacting nearest-neighbor nuclear spins. Our work lays down a foundational step for realizing precise control on near-term quantum hardware that utilizes NV centers, leading to high fidelities.

1. Introduction

The ability to accurately simulate quantum systems, as envisioned by Feynman [1], lies at the forefront of realizing the transformative potential of quantum mechanics. From designing novel materials with exotic properties to understanding fundamental laws of physics and unlocking the mysteries of the universe, quantum simulation's true promise holds the key to revolutionary breakthroughs [2–4]. While the ideal fault torrent quantum computer promises unprecedented accuracy over their classical counterparts – so-called *quantum supremacy* [5] – current utilization of quantum devices is noisy and prone to errors, termed *noisy intermediate-scale quantum* (NISQ) devices [6]. Noise significantly reduces coherence time, limiting our ability to simulate complex quantum systems. This is especially problematic for near-term devices that need more qubits and deeper circuits, as their output cannot always be validated. These challenges have led researchers to rethink algorithm design. Instead of focusing on fault-tolerant algorithms like Shor's prime factorization [7], which promise definitive quantum supremacy, the focus has shifted towards creating new algorithms for current noisy

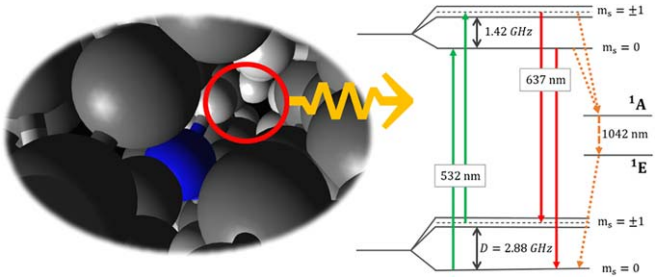

Figure 1. (Left) Diamond lattice structure with a single NV center highlighting the nitrogen atom substitution (blue) and a vacancy (red). (Right) Energy level diagram of the NV center's electronic spin-triplet state (S = 1); the ground state with the zero-field splitting D = 2.88 GHz. The red and green arrows show optical transitions for excitation (532 nm) and emission (637 nm). The dashed orange arrows show a non-radiative decay and an infrared emission pathway (1042 nm) between intermediate singlet states (I_A and I_E).

hardware. The new classes of algorithms are intended to demonstrate a *near-utility* quantum advantage over classical algorithms in specific problems [6].

One promising class of quantum algorithms for near-term applications is Variational Quantum Algorithms (VQAs). VQAs exploit a hybrid quantum-classical (HQC) computational model. In this approach, a quantum processor is employed to estimate the eigenvalues of a parameterized quantum circuit, leveraging quantum superposition and entanglement to achieve an exponential speedup over classical methods [8]. A classical optimizer then iteratively adjusts the quantum circuit parameters to evaluate the lowest eigenvalues of the observables. This iterative feedback loop between quantum and classical components allows VQAs to address complex quantum systems while mitigating noise, decoherence, and errors inherent to NISQ devices [9]. A notable example of VQAs is the variational quantum eigensolver (VQE), which is well-suited for simulating quantum systems in chemistry and materials science [10, 11]. VQEs provide a pathway for bridging the gap between theoretical insights and experimental observations in quantum science. Moreover, other parameterized quantum circuits, such as quantum neural networks (QNNs), have emerged as promising tools for machine learning tasks, including deep learning. While inspired by the success of VQEs, QNNs leverage their adaptive and trainable structures to model quantum interactions efficiently [12].

Nonetheless, the quantum computer is a valuable platform for modeling complex quantum systems, including but not limited to the hyperfine interactions in diamond nitrogen-vacancy (NV) centers. NV centers are point defects in the diamond lattice, consisting of a nitrogen atom that substitutes a carbon atom with a neighboring vacant lattice site (see figure 1). These point defects have emerged as remarkable platforms for quantum technologies due to their unique combination of optical and spin properties, coupled with long coherence times (>1 s) at room temperature [13, 14]. The hyperfine interactions between the NV center's electron spin triplet ($S = 1$) and the nuclear spins of surrounding atoms, particularly the rare ^{13}C isotopes with a nuclear spin of ½, are critical factors influencing the NV center's behavior in quantum sensing and information processing applications. For instance, one promising application of NV center systems is envisaged in nanomagnetometry [15, 16]. However, the complexity of capturing quantum effects in NV centers often overwhelms traditional computational methods, making efficient modeling a challenge. This challenge is more pronounced with anisotropic nuclear spin interactions, which vary in strength and direction based on the relative position of the ^{13}C nuclei to the NV center. Quantum computers, on the other hand, leverage the inherent power of quantum phenomena to provide a more accurate and efficient path for modeling such complex systems [17–20].

Therefore, we introduce a parameterized variational quantum circuit (VQC) inspired by QNN architecture to simulate the NV center's ground state dynamics. The VQC's multi-layered structure enables efficient capture of electron-nuclear spin correlations of the NV center system. It utilizes single-qubit rotations and two-qubit entangling gates to model the Hamiltonian governing the NV center's electron and nuclear spin interactions. The circuit's unitary evolution was approximated by a sequence of *Trotter* steps, with each step utilizing distinct parameter values, thereby establishing a conceptual parallel to the layered structure found in QNNs. Despite this structural similarity, the optimization and training methodologies for our VQC slightly differ from those used in QNNs. However, this approach still affords flexible and efficient simulation of the NV center system, even on NISQ devices. The VQC's observables incorporate the effects of hyperfine interactions between the ^{14}NV electron and a nearby ^{13}C nuclear spin. The ^{14}NV-^{13}C's Hamiltonian is encoded into the VQC ansatz, and its parameters are iteratively optimized to minimize the energy, thus approximating the ^{14}NV-^{13}C's ground state. The optimization process utilizes classical algorithms that analyze measurement outcomes from the quantum processor's qubits.

The findings presented in this work show that QNN-inspired VQCs may effectively model the ground state dynamics of NV centers. Related research on NV center qubit systems simulation neglected anisotropic hyperfine interactions resulting from ^{14}N and ^{13}C spin interactions [21–23]. Some researchers have demonstrated the validity of neural network VQAs in simulating quantum many-body dynamics [24], while others have suggested optimization of the variational QNNs based on collective intelligence [25]. Of keen interest in our present work is the observation that gradient-free classical optimizers are a good candidate for minimizing the designed VQC's cost function in a barren plateau landscape, which is reasonably expected when dealing with randomly initialized ansatz parameters [26–28]. Hence, we have developed an approach to simulate the ^{14}NV-^{13}C Hamiltonian while efficiently accommodating hyperfine quantum effects.

2. Methodology

2.1. System hamiltonian and propagator

The NV center's spin behavior in the presence of external magnetic fields and internal interactions with neighboring atomic nuclei is described by its spin Hamiltonian. For the specific case of a ^{14}NV center interacting with a nearby ^{13}C nucleus, the resulting energy level transitions are governed by the Hamiltonian (H_{NV}) [19]:

$$H_{NV} = \Delta S_z^2 + P(I_z^{(N)})^2 + \mathbf{B}\cdot\ (g\mu_B\mathbf{S} - \gamma_N\mathbf{I^{(N)}} - \gamma_C\mathbf{I^{(C)}}) + \mathbf{S}\cdot\ (\mathbf{A_N}\cdot\mathbf{I^{(N)}} + \mathbf{A_C}\cdot\mathbf{I^{(C)}}) \tag{1}$$

where ΔS_z^2 is the electron *zero-field splitting* in the z-direction (S_z) which is caused by spin-spin interactions within the electron system of the ^{14}NV center. $\Delta \approx 2.87GHz$ is the electronic zero-field splitting parameter. The ^{14}NV center has a nuclear spin $l = 1$ resulting in a non-zero quadrupole moment. Hence, the interaction of the nuclear quadrupole moment with the electric field gradient created by the surrounding crystal lattice is described by the term $P(I_z^{(N)})^2$which is essentially the *nuclear quadrupole interaction* of the ^{14}NV nuclear spin in the z-direction ($I_z^{(N)}$) and $P \approx -5MHz$ is the ^{14}NV quadrupole coupling constant. The term $\mathbf{B}\cdot\ (g\mu_B\mathbf{S} - \gamma_N\mathbf{I^{(N)}} - \gamma_C\mathbf{I^{(C)}})$ represents the *Zeeman interaction* of the ^{14}NV-^{13}C system's electron spin ($\mathbf{S}$), ^{14}NV nuclear spin ($\mathbf{I^{(N)}}$) and the ^{13}C nuclear spin ($\mathbf{I^{(C)}}$) with an external magnetic field ($\mathbf{B}$). The electron *g-factor* $g = g_| = 2.0029$ lies along the $\langle 111\rangle$ ^{14}NV symmetry axis, whereas the coefficient $\mu_B \approx 5.788 \times 10^{-5}eV/T$ is the Bohr magneton. The last term $\mathbf{S}\cdot\ (\mathbf{A_N}\cdot\mathbf{I^{(N)}} + \mathbf{A_C}\cdot\mathbf{I^{(C)}})$ represents the *hyperfine interactions* between the electron and the ^{14}NV-^{13}C nuclear spins.
$\mathbf{A_N}$ ($\mathbf{A_{N|}} \approx -2.16MHz; \mathbf{A_{N\perp}} \approx -2.70MHz$) and $\mathbf{A_C}$ ($\mathbf{A_{C|}} \approx 199.7\ MHz; \mathbf{A_{C\perp}} \approx 120.3\ MHz$) are the hyperfine tensors and $\gamma_N = 1.933 \times 10^7 rad{\cdot}T^{-1}s^{-1}$ $(\gamma_N/2\pi = 307.7Hz\ \cdot\ G^{-1})$ and $\gamma_C = 6.7261 \times 10^7 rad{\cdot}T^{-1}s^{-1}$ $(\gamma_C/2\pi = 1.0705kHz\ \cdot\ G^{-1})$ are the gyromagnetic ratios for the ^{14}N and ^{13}C nuclear spins, respectively [21, 29–32].

The Schrödinger's time-dependent equation may be used to describe the evolution of the ^{14}NV-^{13}C system's initial state, $|\psi(t_0)\rangle$ (see Appendix A: [33]). Then, we define the time evolution unitary operator (i.e., propagator) $\hat{U}(t,\ t_0)$ which will help us to realize the dynamical evolution of the initial state to some other final state, $|\psi(t)\rangle$, at a later time t. Taking $t_0 = 0$ and the reduced Plank's constant $\hbar = 1$, we get:

$$i\hbar\frac{\partial}{\partial t}[\hat{U}(t,\ t_0)\ |\psi(t_0)\rangle] = \hat{H}_{NV}[\hat{U}(t,\ t_0)\ |\psi(t_0)\rangle] = \hat{H}_{NV}\ |\psi(t)\rangle \text{ for } t > t_0 \tag{2}$$

$$\Rightarrow\ |\psi(t)\rangle = e^{-\left[\frac{i}{\hbar}\hat{H}_{NV}(t-t_0)\right]}\ |\psi(t_0)\rangle = e^{-i\hat{H}_{NV}t}\ |\psi(0)\rangle \tag{3}$$

where $|\psi(0)\rangle$ is the initial state of the ^{14}NV-^{13}C system and $\hat{U}(t) = e^{-i\hat{H}_{NV}t}$ is the propagator representing a finite (or discrete) time translation. Since we know all elements of $\hat{H}_{NV}$, we can expand the exponential terms of the propagator as follows:

$$\hat{U}(t) = e^{-i[\Delta S_z^2 + P(I_z^{(N)})^2 + \mathbf{B}\cdot\ (g\mu_B\mathbf{S} - \gamma_N\mathbf{I^{(N)}} - \gamma_C\mathbf{I^{(C)}}) + \mathbf{S}\cdot\ (\mathbf{A_N}\cdot\mathbf{I^{(N)}} + \mathbf{A_C}\cdot\mathbf{I^{(C)}})]t} \tag{4}$$

$$\therefore \hat{U}(t) = \hat{U}_\Delta(t)\,\hat{U}_P(t)\,\hat{U}_{\mu_B}(t)\,\hat{U}_{\gamma_N}(t)\,\hat{U}_{\gamma_C}(t)\,\hat{U}_{\mathbf{A_N}}(t)\,\hat{U}_{\mathbf{A_C}}(t) \tag{5}$$

Where $\hat{U}_\Delta(t) = e^{-i(\Delta S_z^2)t}$ is the Zero-field splitting operator of the electron spin (S_z); $\hat{U}_P(t) = e^{-i[P(I_z^{(N)})^2]t}$ is the *Quadrupole interaction operator* of the ^{14}N nuclear spin ($I_z^{(N)}$); $\hat{U}_{\mu_B}(t) = e^{-i[\mathbf{B}\cdot(g\mu_B\mathbf{S})]t}$ is the *Zeeman interaction operator* of the electron spin ($\mathbf{S}$); $\hat{U}_{\gamma_N}(t) = e^{i[\mathbf{B}\cdot\ (\gamma_N\mathbf{I^{(N)}})]t}$ is the *Zeeman interaction operator* of the ^{14}N nuclear spin; $\hat{U}_{\gamma_C}(t) = e^{i[\mathbf{B}\cdot(\gamma_C\mathbf{I^{(C)}})]t}$ is the Zeeman interaction operator of the ^{13}C nuclear spin; $\hat{U}_{\mathbf{A_N}}(t) = e^{-i[\mathbf{S}\cdot(\mathbf{A_N}\cdot\mathbf{I^{(N)}})]t}$ is the *Anisotropic hyperfine interaction operator* between the ^{14}NV electron spin ($\mathbf{S}$) and the ^{14}N nuclear spin ($\mathbf{I^{(N)}}$); and $\hat{U}_{\mathbf{A_C}}(t) = e^{-i[\mathbf{S}\cdot(\mathbf{A_C}\cdot\mathbf{I^{(C)}})]t}$ is the *Anisotropic hyperfine interaction operator* between the NV electron spin ($\mathbf{S}$) and the ^{13}C nuclear spin ($\mathbf{I^{(C)}}$).

2.2. Hamiltonian encoding

Having established a well-defined time evolution unitary operator $\hat{U}(t)$, as shown in equation (4 & 5), simulation of the ^{14}NV-^{13}C Hamiltonian is now transformed into the task of constructing a quantum circuit representation for the propagator, which can be realized using quantum gates. In this section, we aim to translate the Hamiltonian into a VQC observable, where each term in equation (5) corresponds to a unique unitary

operator. This allows us to map the propagator into a sequence of single-qubit Pauli rotation and two-qubit entangling gates by extracting individual matrices of the propagator components $\hat{U}_i(t)$ into their equivalent quantum gates. This approach necessitates a sequential treatment of evolution time to achieve higher accuracy in simulating the spin dynamics of the ^{14}NV-^{13}C system. As a first step, we consider the first-order *Trotter-Suzuki* decomposition of the propagator for the system Hamiltonian, as presented in equations (6–8). A similar technique was employed in [34], where a *2D Transverse Field Ising Model Hamiltonian* was utilized instead.

$$\hat{U}(\delta t) = e^{-i\hat{H}_{NV}\delta t} \approx \prod_j e^{-i\hat{H}_{NV\,j}\delta t} \tag{6}$$

$$\begin{aligned}\hat{U}(\delta t) = {} & e^{-i(\Delta S_z^2)\delta t} \cdot e^{-i[P(I_z^{(N)})^2]\delta t} \cdot e^{-i[\boldsymbol{B}\cdot(g\mu_B \boldsymbol{S})]\delta t} \\ & \cdot e^{i[\boldsymbol{B}\cdot(\gamma_N \boldsymbol{I}^{(N)})]\delta t} \cdot e^{i[\boldsymbol{B}\cdot(\gamma_C \boldsymbol{I}^{(C)})]\delta t} \\ & \cdot e^{-i[\boldsymbol{S}\cdot(\boldsymbol{A}_N\cdot\boldsymbol{I}^{(N)})]\delta t} \cdot e^{-i[\boldsymbol{S}\cdot(\boldsymbol{A}_C\cdot\boldsymbol{I}^{(C)})]\delta t}\end{aligned} \tag{7}$$

$$\Rightarrow \quad \hat{U}(\delta t) = \hat{U}_\Delta(\delta t)\hat{U}_P(\delta t)\hat{U}_{\mu_B}(\delta t)\hat{U}_{\gamma_N}(\delta t)\hat{U}_{\gamma_C}(\delta t)\hat{U}_{\mathbf{A}_N}(\delta t)\hat{U}_{\mathbf{A}_C}(\delta t) \tag{8}$$

Each decomposition in equation (8) represents a distinct unitary operator that contributes to the overall effect of the propagator $[\hat{U}(\delta t) = \prod_i \hat{U}_i(\delta t)]$, evolving the initial ^{14}NV-^{13}C state $|\psi(0)\rangle$ into an intermediate state $|\psi(\delta t)\rangle$ within a short time step δt. This process discretizes the total evolution time t into a finite number of $n = t/\delta t$ *Trotter* steps $[\hat{U}(t) \approx e^{(-i\hat{H}_{NV}\delta t)n}]$ which corresponds to the number of iterations for the classical optimization steps. Then, the constituent operators of the *Trotterized propagator* are translated into a sequence of single- and two-qubit gates, forming the fundamental building blocks of the VQC ansatz.

To affect the Hamiltonian encoding, we consider the magnetic field $\boldsymbol{B}$ to be directed along the $z-axis$ (such that $\boldsymbol{B} \equiv B_z$) and this constraint greatly simplifies the step-wise propagator $\hat{U}(\delta t)$. Thus, we further apply the Bravyi-Kitaev Transformation (BKT) [35] to map the $\hat{U}_j$ terms of the *Trotterised propagator* to their approximated qubit operators [35, 36]. This treatment is suitable for the large size of the ^{14}NV-^{13}C Hamiltonian in equation (1) because the quantum circuit depth has to be kept shallow for optimal simulation. The BKT's quantum gate encoding is implemented as shown in equations (9–15) by transforming the electron and nuclear spin operators S_z, $I_z^{(N)}$, $I_z^{(C)}$ to qubit operators $Q_z = \frac{1}{2}Z_i = \frac{1}{2}I_i$, where i is the corresponding qubit index.

$$\hat{U}_\Delta(\delta t) \equiv P_{(e)}\left(\frac{\Delta}{2}\delta t\right) = P_{(e)}(\theta_\Delta) \tag{9}$$

$$\hat{U}_P(\delta t) \equiv P_{(N)}\left(\frac{P}{2}\delta t\right) = P_{(N)}(\theta_P) \tag{10}$$

$$\hat{U}_{\mu_B}(\delta t) \equiv R_{Z_e}(g\mu_B B_z \delta t) = R_{z_e}(\theta_{\mu_B}) \tag{11}$$

$$\hat{U}_{\gamma_N}(\delta t) \equiv R_{Z_N}(-\gamma_N B_z \delta t) = R_{z_N}(\theta_{\gamma_N}) \tag{12}$$

$$\hat{U}_{\gamma_C}(\delta t) \equiv R_{Z_C}(-\gamma B_z \delta t) = R_{Z_C}(\theta_{\gamma_C}) \tag{13}$$

$$\hat{U}_{\mathbf{A}_N}(\delta t) \approx \prod_{j\langle x,y,z\rangle} e^{-i(S_j\cdot A_{Nj,j}\cdot I_j^{(N)})\delta t} \equiv \prod_{j\langle x,y,z\rangle} R_{j_e j_N}\left(\frac{A_{Njj}}{2}\right) \tag{14}$$

$$\hat{U}_{\mathbf{A}_C}(\delta t) \approx \prod_{j\langle x,y,z\rangle} e^{-i(S_j\cdot A_{Nj,j}\cdot I_j^{(c)})\delta t} \equiv \prod_{j\langle x,y,z\rangle} R_{j_e j_c}\left(\frac{A_{cjj}}{2}\right) \tag{15}$$

where $P_{G(e)}$ and $P_{G(N)}$ are single-qubit phase gates for the electron and ^{14}N nuclear spin qubits; R_{z_e}, R_{z_N} and R_{z_C} are the *z-axis* single-qubit rotation gates for the electron, ^{14}N, and ^{13}C qubits respectively. $\prod_{j\langle x,y,z\rangle} R_{j_e j_N}\left(\frac{A_{Nij}}{4}\right)$ and $\prod_{j\langle x,y,z\rangle} R_{j_e j_C}\left(\frac{A_{Cjj}}{4}\right)$ represents two-qubit rotation gates for the electron, ^{14}N, and ^{13}C qubits with three degrees of freedom $j \in \{x, y, z\}$.

By using the encoding described in equations (9–15), the ^{14}NV-^{13}C Hamiltonian was then translated into the VQC circuit as an observable made up of quantum gates shown in equation (16) (see Appendix A for full proof and Appendix B for encodings and parameter definitions).

$$\begin{aligned}\hat{H}_{NV} = {} & \left(\tfrac{\Delta}{4}\right)I_e + \left(\tfrac{P}{4}\right)I_N + \left(\tfrac{g\mu_B B_z}{2}\right)Z_e - \left(\tfrac{\gamma_N B_z}{2}\right)Z_N - \left(\tfrac{\gamma B_z}{2}\right)Z_C \\ & + \left[\left(\tfrac{A_{Nxx}}{4}\right)X_eX_N + \left(\tfrac{A_{Nyy}}{4}\right)Y_eY_N + \left(\tfrac{A_{Nzz}}{4}\right)Z_eZ_N\right] + \left[\left(\tfrac{A_{Cxx}}{4}\right)X_eX_C + \left(\tfrac{A_{Cyy}}{4}\right)Y_eY_C + \left(\tfrac{A_{Czz}}{4}\right)Z_eZ_N\right]\end{aligned} \tag{16}$$

While aligning the external magnetic field with the *z-axis* simplified the *Trotterized propagator*, we intentionally chose not to diagonalize the hyperfine tensors A_{Njj} (A_{Cjj}) in the VQC observable to avoid

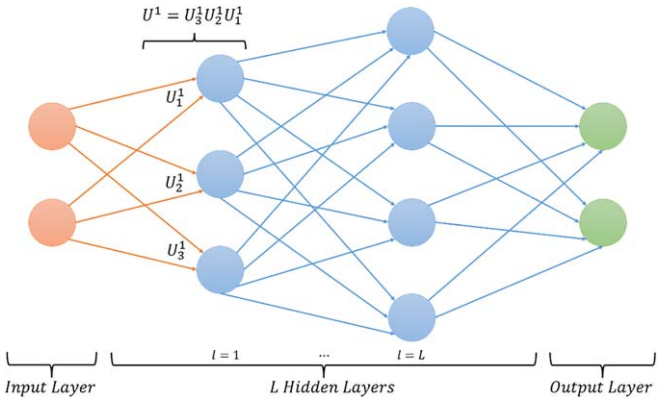

Figure 2. A quantum feedforward neural network architecture with an input, an output, and L hidden layers. The number of hidden layers L represents the intermediate quantum states of the QNN circuit and determines network depth. The input and output layers represent the initial and final quantum states of the QNN circuit respectively (adapted from figure 1 in [12] and figure 2 in [37]).

oversimplification. This is because their off-diagonal elements are crucial for capturing the desired ^{14}NV-^{13}C system hyperfine interactions between the electron and nuclear spins.

2.3. QNN-inspired architecture of the VQC

A quantum neural network (QNN) is a quantum circuit composed of quantum perceptrons, the quantum equivalent of perceptrons in classical machine learning. It consists of L hidden qubit layers acting on an initial state (ρ^{in}) of the input qubits, and producing a final, potentially mixed state (ρ^{out}) for the output qubits, as described by equation (17) [12, 37]:

$$\rho^{out} \equiv \text{tr}_{\text{in,hid}}(u(\rho^{in} \otimes |0 \cdots 0\rangle_{\text{hid,out}} \langle 0 \cdots 0) u^{+}), \tag{17}$$

where $u \equiv U^{\text{out}} U^{L} U^{L-1} \cdots U^{1}$ is the QNN quantum circuit, U^{l} represents the unitary operator of the l^{th} QNN layer, comprised of a product of quantum perceptrons (or neurons) acting on the qubits in layers l-1 and l, and $\text{tr}_{\text{in,hid}}$ is the partial trace operation over the input (in) and hidden (hid) qubits. So, for a typical quantum feedforward neural network architecture, we have an *input*, an *output*, and *L hidden layers* as shown in figure 2.

Thus, our QNN-inspired VQC circuit layout is designed to simulate the ^{14}NV center Hamiltonian with a proximal ^{13}C isotope. This architecture leverages the quantum neural network (QNN) concepts introduced above to encode and optimize the Hamiltonian for efficient simulation. The VQC circuit has three main components: (a) the *input layer* which is defined by 3-qubit entanglement initialization protocols [i.e. $|\text{GHZ}\rangle_3$ and $|\text{W}\rangle_3$ states in equation (18)] operated by the U_R unitary on three quantum registers; (b) *L hidden layers* which represent the parameterized parts of the variational form of the VQC, and it is embedded with trainable theta parameters that act as inputs to the U_V^l operator on each circuit layer (note that the *input layer* and *L hidden layers* constitute the VQC ansatz); and (c) the *output layer* which denotes the result of ansatz measurement that can be stored on classical registers for optimization and further processing (see illustration in figure 3).

$$|\text{GHZ}\rangle_3 = \frac{1}{\sqrt{2}}(|000\rangle + |111\rangle); \text{ and}$$
$$|\text{W}\rangle_3 = \frac{1}{\sqrt{3}}(|001\rangle + |010\rangle + |100\rangle) \tag{18}$$

The classical optimization process iteratively adjusts theta parameters of the parameter vector to minimize the VQC's cost function. The ^{14}NV-^{13}C Hamiltonian $\hat{H}_{NV}$ in equation (1) was encoded as an observable of the VQC circuit in equation (16) and the cost function f_c minimized the expectation values of the observable as shown in equation (19).

$$f_c(\vec{\theta}) = \xrightarrow[\vec{\theta}]{\arg\min} \langle \psi(\vec{\theta}) | \hat{H}_{NV} | \psi(\vec{\theta}) \rangle \tag{19}$$

where $\vec{\theta}$ is the parameter vector of the VQC, $f_c(\vec{\theta})$ is the cost function with input $\vec{\theta}$, $|\psi(\vec{\theta})\rangle$ is the VQC ansatz's quantum state prepared with n theta parameters of the parameter vector $\vec{\theta}(\vec{\theta}_1 \cdots \vec{\theta}_n)$, and $\langle \psi(\vec{\theta}) | \hat{H}_{NV} | \psi(\vec{\theta}) \rangle$ is the expectation value of $\hat{H}_{NV}$ for the VQC ansatz state $|\psi(\vec{\theta})\rangle$.

The VQC [figure 3 (left)] is purposely tailored to evaluate the ground state energy of the ^{14}NV-^{13}C system. To achieve this, we utilize the cost function in equation (19) to evaluate the expectation value of the Hamiltonian. This expectation value is then fed into a classical optimizer, which iteratively adjusts the parameters of our quantum circuit to minimize the cost function. For instance, in the case of a gradient-based optimizer, as

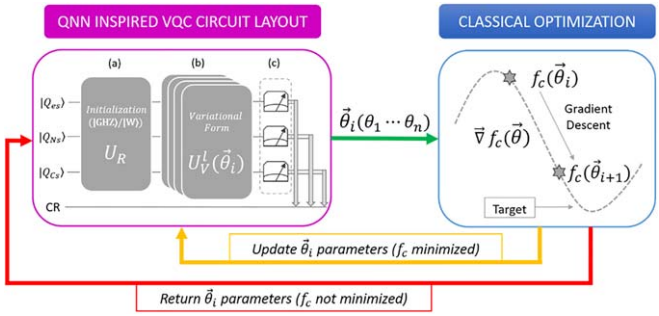

Figure 3. A QNN-inspired VQC architecture designed to simulate the ^{14}NV-^{13}C Hamiltonian. The VQC configuration (left) consist of (a) an input layer where qubits are initialized using the entangling GHZ_3 and W_3 states; (b) hidden layers comprising the variational form, parameterized with single-qubit Pauli rotations and 2-qubit entangling CNOT gates, which encode the Hamiltonian as an ansatz observable; and (c) an output layer where measurements are taken. The classical optimization process (right) iteratively adjusts theta parameters of the parameter vector $\vec{\theta}_i(\theta_1 \cdots \theta_n)$ to minimize the cost function $f_c(\vec{\theta}_i)$ via gradient descent. Ansatz theta parameters are updated only if the cost function is minimized. The optimization process continues until convergence to the target value is achieved or when a maximum iteration limit is exceeded. The feedback loop (green, yellow, and red arrows) demonstrates the iterative nature of optimization, where circuit parameters for each subsequent QNN layer are conditionally updated.

depicted under classical optimization in figure 3 (right), the parameters are adjusted iteratively by defining the gradient of the cost function $\vec{\nabla} f_c(\vec{\theta})$ at an initial point with a parameter vector $\vec{\theta}_i$, and then following through the direction of the steepest descent. The next sets of parameters are then updated as follows: $\vec{\theta}_{i+1} = \vec{\theta}_i - \eta \vec{\nabla} \ f_c(\vec{\theta})$, where η is the learning rate comparable to *Trotter* steps [27, 38, 39].

Upon successful optimization, we obtain a set of optimized parameters, $\vec{\theta}^*(\theta_1^* \cdots \theta_n^*)$. These parameters define the optimal VQC ansatz configuration, allowing us to construct and approximate the ground state wavefunction, $|\psi(0)\rangle \approx |\psi(\vec{\theta}^*)\rangle$. By measuring this state, we directly obtain the ground state energy eigenvalues, $f_c(\vec{\theta}^*)$, of the ^{14}NV-^{13}C system. This hybrid approach harnesses the power of quantum computation to represent and manipulate quantum states, while leveraging classical optimization techniques to efficiently find the solution.

2.4. VQC design and Initialization

We designed the VQC circuit using IBM's Qiskit SDK in Python to validate our approach. Three quantum registers denoted as Q^{es}, Q^{Ns}, and QCs for the NV center's electron spin, ^{14}N, and ^{13}C nuclear spins, respectively, were used to represent the qubit states of the VQC. Measurements (meas) on the three spin qubits were stored on three classical registers: CRes, CRNs, and CRCs, respectively. The VQC was initialized in the GHZ_3 and W_3 states to create an entangled reference quantum circuit for the three qubits [40, 41]. The *Hinton*, *Q-sphere*, and State City plots for the 3-qubit initialization protocols are shown in figures 5 (b) and (c). A parameterized variational form of the quantum circuit was created using a *Hardware Efficient SU(2) 2-local circuit (ESU2)* and then integrated with the initialized reference circuits to compose the final VQC ansatz. ESU2 is based on the Two-Local circuit, a parameterized circuit composed of alternating rotation and entanglement layers [42]. In this case, ESU2 circuit design was used to implement single qubit operations spanned by SU(2) and CX entanglements, resulting in a heuristic pattern useful in preparing trial wave functions for VQCs. SU(2) refers to a special unitary group of degree 2, whose elements are 2×2 unitary matrices with determinant 1, e.g. Pauli rotation gates [43]. The parameter vector $\vec{\theta}$ had 24 theta parameters, which were fed into the ESU2 ansatz as trainable variational inputs of the variational unitary U_V^l. The complete VQC circuit design is shown in figure 4, with *four hidden layers* of the variational circuit.

The final VQC circuit was successfully run on the 127-qubit IBM quantum hardware, *ibm_brisbane*, using BackendEstimatorV2 [44]. The quantum processing unit's (QPU) qubit lattice connectivity is visually represented with a color gradient, indicating the error probabilities associated with single and two-qubit gates. Lighter colors signify higher error rates, while darker colors indicate lower ones, as depicted in figure 5(a). The median error rates for ECR, SX, and readout operations were 7.814×10^{-3}, 2.359×10^{-4}, and 1.330×10^{-4}, respectively. The QPU's qubit topology allowed our 3-qubit chain VQC design to achieve a low error rate of about 3.2% per layered gate [45]. We further suppressed and mitigated errors by adjusting the resilience and optimization levels of Qiskit's runtime primitives to reduce the impact of noise and enhance optimization efficiency.

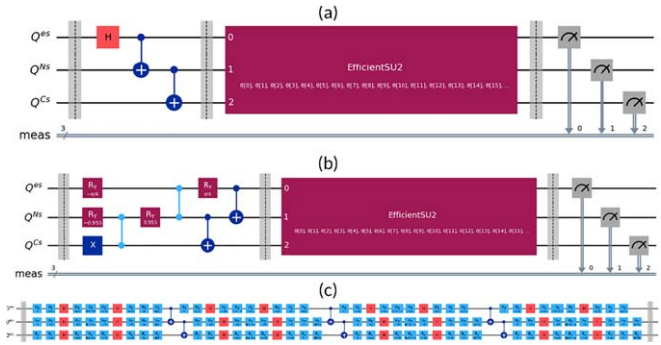

Figure 4. Design of the VQC ESU2 ansatz circuit. The ansatz is initialized with GHZ_3 and W_3 states, in (a) and (b) respectively, acting as the *input layer*. (c) Transpiled ESU2 variational form with *4 hidden layers* comprised of 24 theta parameters as inputs of the variational unitary operator U_V^l. Results of measurement on the three spin qubits in (a) and (b) are stored on 3 classical registers (meas) representing the *output layer*.

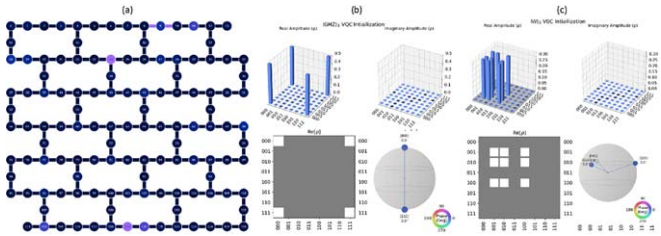

Figure 5. (a) Topology graph for the 127-qubit *ibm_brisbane* quantum hardware. The qubit lattice connectivity for the quantum processing unit (QPU) is visually represented with a color gradient indicating error probabilities associated with single and 2-qubit gates. Lighter colors signify higher error rates, while darker ones signify lower error rates. Parts (b) and (c) depict the Hinton, Q-sphere, and State City plots for the GHZ_3 and W_3 initialization protocols. The VQC's reference circuit is initialized with pure quantum states.

3. Results and discussion

3.1. VQC ansatz optimization

The VQC's ansatz parameters were optimized using six classical optimization algorithms to ascertain their suitability for efficiently minimizing the eigenvalues of the cost function. In particular, we trial-tested three gradient-based (BFGS, L-BFGS-B, *and ADAM)* and three gradient-free *(COBYLA, POWELL, and NELDER-MEAD)* classical optimizers. We initiated the optimization process by generating six different instances of pseudo-random parameter vectors $\{\vec{\theta}_1, \vec{\theta}_2,\cdots,\vec{\theta}_6\}$, with each parameter vector having 24 trainable theta parameters [i.e. $\vec{\theta}_i(\theta_1, \theta_2,\cdots,\theta_{24})$] as inputs to the ansatz's l^{th} variational unitary $U_V^l(\vec{\theta}_i)$. Each l^{th} unitary operation corresponded to a unique quantum state of the VQC's ansatz for each optimization loop. Each of the six randomly initialized parameter vectors was subjected to optimization using the selected classical algorithms. By taking $\delta t = 0.002$ and $\boldsymbol{B} \equiv B_z = 1\text{T}$, the six classical optimization algorithms were then run for every initial pseudo-random parameter vector $(\vec{\theta}_i)$ in tandem with the VQE's cost function, which evaluated eigenvalues for a maximum of 500 optimization steps (or up until the point of convergence to the target). These optimization pathways are visualized in figure 6.

Optimization results in figure 6 show that only three non-gradient optimization algorithms (i.e., COBYLA, POWELL, and NELDER-MEAD) were successful at minimizing the estimated energy eigenvalues evaluated by the VQC's cost function operating, which operated on the circuit observable. Of these three, COBYLA was the quickest optimizer and reached the minimum eigenvalues within the first 300 optimization steps. The other three gradient-based optimizers (BFGS, L-BFGS-B, and ADAM) failed to minimize the cost function, possibly due to the existence of barren plateaus on the optimization landscape, which is attributable to parameterized circuits initialized with random initial parameter values [26–28]. Since barren plateau landscapes are quite common and diminish the continuity of gradient descent when implementing gradient-based optimization algorithms, researchers have proposed techniques for avoiding their occurrence by using classical shadows [46], classical deep neural networks [47], trainable Fourier coefficients of Hamiltonian system parameters [48], and transfer-learning-inspired parameter initializations [49] among others.

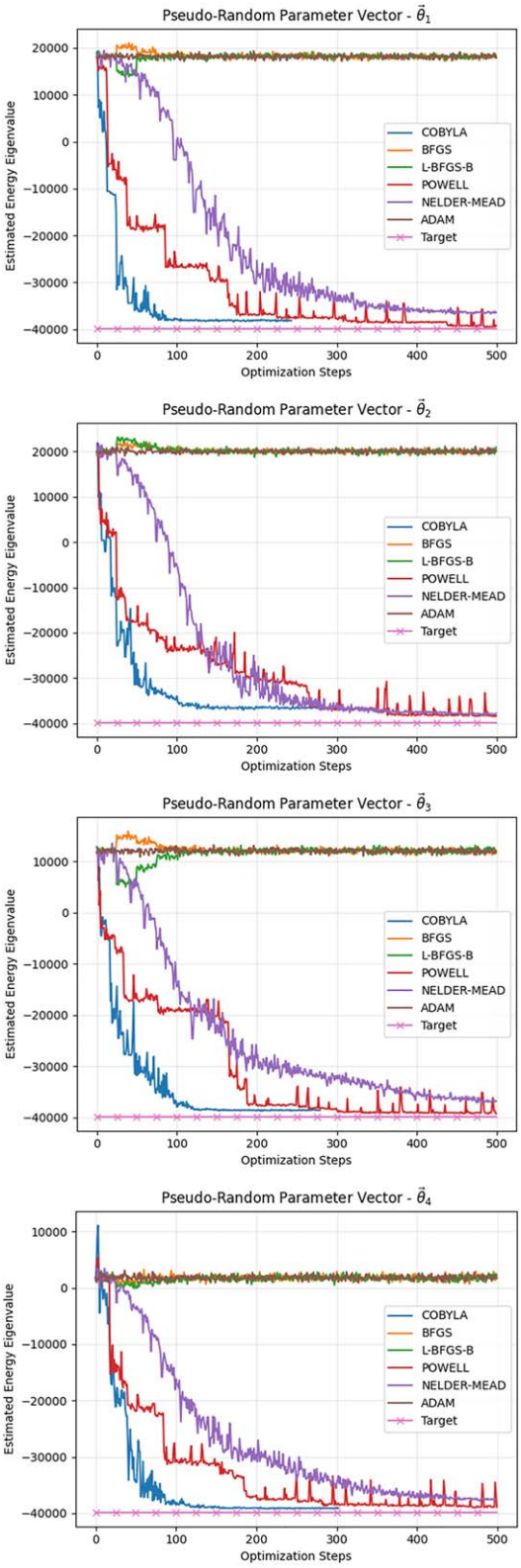

Figure 6. Plots of six classical optimization algorithm pathways for the VQC ansatz. The optimizers were run for six different initial pseudo-random parameter vectors $\{\vec{\theta}_1, \vec{\theta}_2, \cdots, \vec{\theta}_6\}$ in tandem with the VQE's cost function, which evaluated eigenvalues for a maximum of 500 optimization steps (or up until the point of convergence to the target). Three gradient-free classical optimizers (COBYLA, POWEL, and NELDER-MEAD) successfully minimized the estimated energy eigenvalues of the VQC's cost function. The other three gradient-based optimizers (BFGS, L-BFGS-B, and ADAM) failed to minimize the cost function, possibly due to the existence of a barren plateau optimization landscape that prevented continuity of gradient descent (see Appendix C for optimization data files).

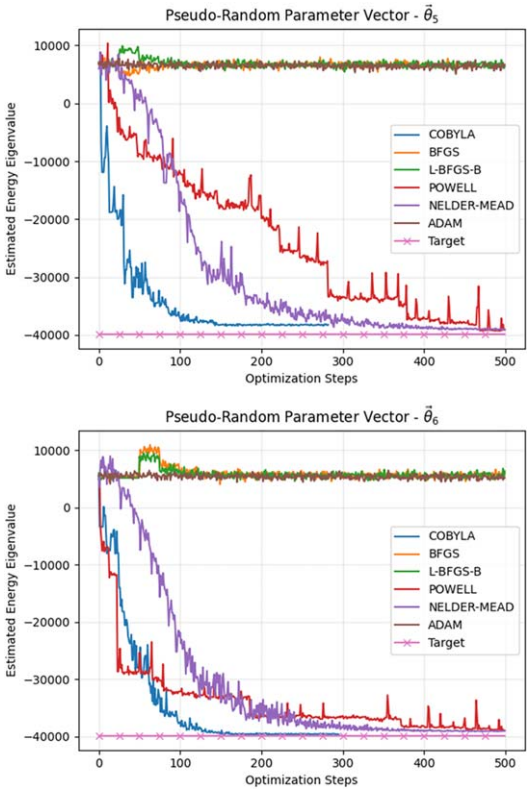

Figure 6. (Continued.)

3.2. Optimal parameters and quasi probability

Each of the 24 theta parameters corresponding to the six sets of the most optimal parameter vectors $\{\vec{\theta}_1^*, \vec{\theta}_2^*, \cdots, \vec{\theta}_6^*\}$, for the three successful algorithms were plotted along with their initial ESU2 pseudo-random theta parameters for both the GHZ_3 and W_3 initialization protocols as presented in figure 7.

Here we see that the optimal parameters for the GHZ_3 initialized ansatz were relatively more diverged from the initial ones as compared to the ones initialized with the W_3 state. While the GHZ_3 initialized state was maximally entangled, the W_3 initialization ensured a genuine multipartite entanglement scheme [see equation (18)], which builds more resilience towards qubit losses in noisy systems [49, 50]. Interestingly, the final states of the most optimal parameter vectors for the GHZ_3 initialized VQC converged at a completely different but maximally entangled state with negligible overlaps, thereby preserving the maximal entanglement scheme which is reportedly shown as a critical component for optimizing quantum circuits [51]. This final state, $|\psi(t)\rangle_f \cong \frac{1}{\sqrt{2}}(|001\rangle + |100\rangle)$, corresponds to the ground state of the NV center system. So, equation (20) represents the complete evolution of spin states for the GHZ_3 initialized ansatz.

$$|\psi(0)\rangle_i = \frac{1}{\sqrt{2}}(|000\rangle + |111\rangle) \Rightarrow |\psi(t)\rangle_f \cong \frac{1}{\sqrt{2}}(|001\rangle + |100\rangle) \tag{20}$$

For the W_3 initialization, the final parameters vectors converged in an almost mixed product state, thus losing their initial entanglement scheme. These observations are confirmable with the results of ESU2 ansatz state vector counts presented as quasi probabilities in figure 8.

3.3. Estimating ^{14}NV-^{13}C ground state

Three sets of optimal ESU2 ansatz parameter vectors (i.e. $\vec{\theta}_{CB}^*$, $\vec{\theta}_{NM}^*$, and $\vec{\theta}_{PO}^*$) were used to obtain their corresponding optimal ansatz state vectors for the COBYLA, NELDER-MEAD, and POWELL optimizers, respectively. Then, state vector Q-spheres and Hinton plots were generated for the initial and each of three optimal ansatz states, as shown in figure 9 (top and bottom, respectively), to track the ^{14}NV-electron spin state transitions. The real Hinton plots for the three successful optimizers indicate that the most optimally probable quantum spin states were the $|001\rangle$ and $|100\rangle$ maximally entangled states. The observed optimal ESU2 ansatz state conforms with the results of the most optimal parameter vectors across the three optimizers as visualized by

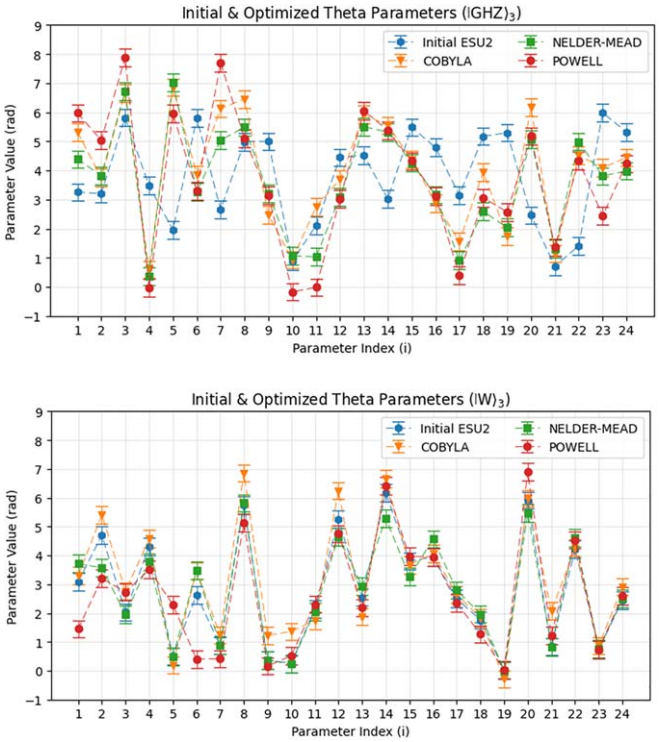

Figure 7. Comparison between the initial pseudo-random and the final optimal parameter vectors (each with 24 theta parameters measured in radians) of the ESU2 ansatz initialized in the $|\,\mathrm{GHZ}\rangle_3$ (top) and $|\,\mathrm{W}\rangle_3$ states (bottom).

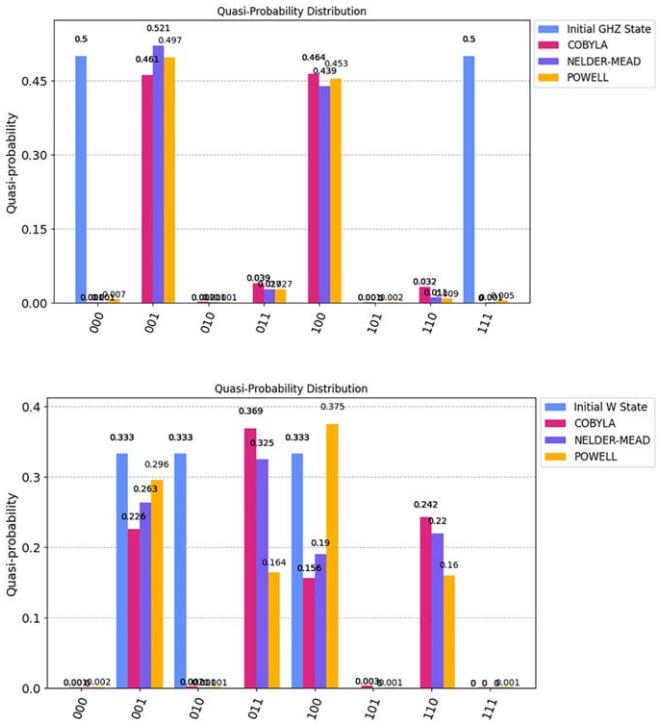

Figure 8. Quasi probability distribution of the initialization protocols and ESU2 ansatz state vectors at optimal theta parameters for the three successful optimization algorithms. The ESU2 ansatz was transpiled using the *Instruction Set Architecture* (ISA) through which state vector probabilities were determined. The ESU2 ansatz circuit was first initialized in the $|\,\mathrm{GHZ}\rangle_3$ state (top) to obtain a maximally entangled reference circuit, resulting in an approximate optimal ansatz state for each optimizer. Then, the ESU2 ansatz was initialized in the $|\,\mathrm{W}\rangle_3$ state (bottom) to obtain a genuine multipartite entangled reference state. With this routine, the final ansatz states converged in an almost mixed product state, thus losing its initial entanglement scheme.

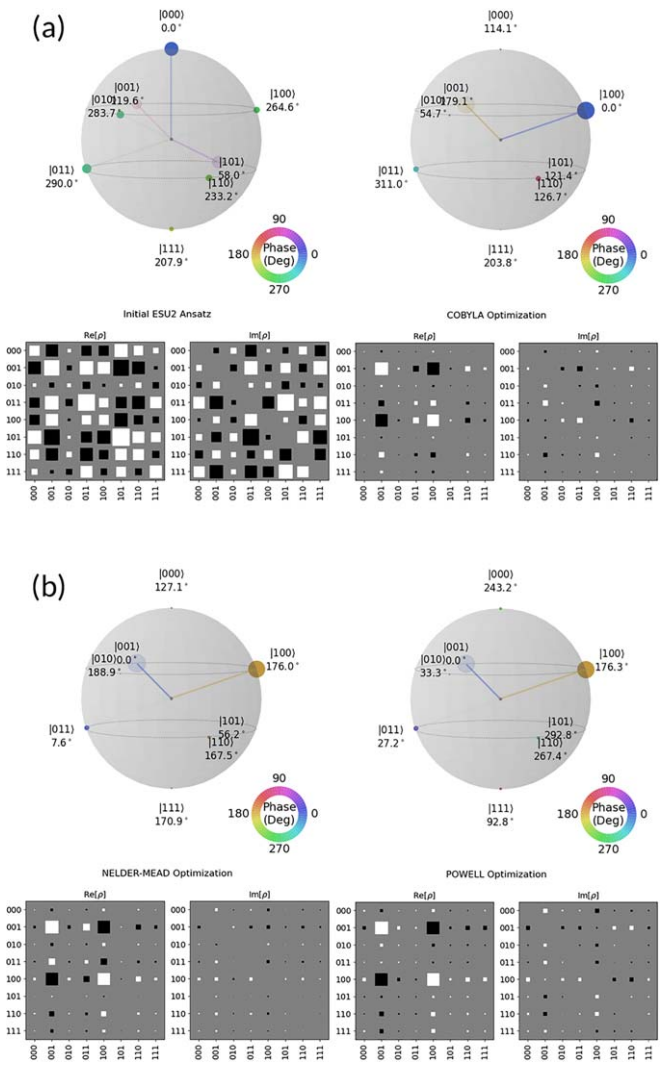

Figure 9. Multi-layered VQC's State vector Q-spheres and Hinton plots, on top and bottom parts in (a) and (b) respectively, for the initial (transpiled) and optimized ESU2 ansatz initialized in the $|\,\mathrm{GHZ}\rangle_3$ state. The real Hinton plots for the COBYLA, NELDER-MEAD, and POWELL optimizers indicates that $|\,001\rangle$ and $|\,100\rangle$ were the most optimally probable spin states corresponding to the ground state $|\,\psi(t)\rangle \cong \frac{1}{\sqrt{2}}(|\,001\rangle + |\,100\rangle)$. The optimal states of the ESU2 ansatz state conforms with the results of optimal parameters across the three optimizers for the quasi-state vector probability distribution in figure 8 (top).

the quasi-state vector probability distribution in figure 8 (left). Hence, the optimal ESU2 ansatz states, obtained through the three classical optimizers, represent our best estimates of the ^{14}NV-^{13}C system's ground states. This correspondence is inherently validated through the VQC's design, where the system Hamiltonian ($\hat{H}_{\mathrm{NV}}$) is encoded as an observable used to minimize the cost function during optimization. In this case, the minimum expectation value of the Hamiltonian, min $\langle\psi(\vec{\theta}^{*})|\hat{H}_{NV}|\psi(\vec{\theta}^{*})\rangle$, is interpreted as the estimated minimum energy eigenvalue of the cost function, which corresponds to the ^{14}NV-electron ground state energy in proximal with a nucleus of ^{13}C isotope.

We also managed to run a single-layer VQC with iterative execution shots to establish if the multi-layered QNN inspired VQC architecture had any observable effect on the optimization efficiency and quantum purity of the final ansatz state vectors as depicted by the state vector Q-spheres and Hinton plots in figure 10. Comparing the results obtained in figures 9 and 10, we notice that the degree of noise in the final ansatz state vectors of each optimization protocol increased drastically when the propagator wasn't Trotterized, thus leading to an inefficient ansatz optimization process.

We further observe that the real and imaginary Hinton plots for the COBYLA, NELDER-MEAD, and POWELL optimizers showed that each of the final VQC ansatz state vectors lost their quantum purity (mainly due to noise) for every optimization pathway. Each optimizer resulted into a completely different and mixed final ansatz state vector, despite having been initialized in the maximally entangled GHZ_3 state. Hence, the noise introduced by running a bulky and single layered VQC on the near term QPU greatly compromised the possibility of reaching a final pure ansatz state. Therefore, with high levels of noise and impure ansatz states, as

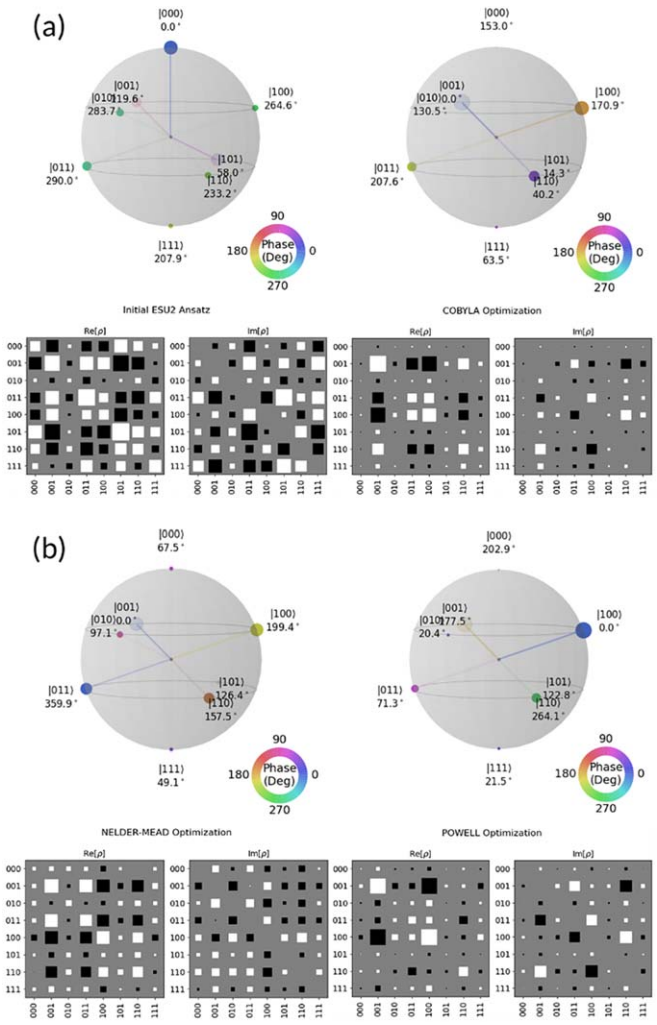

Figure 10. Single layer VQC's State vector Q-spheres and Hinton plots, on top and bottom parts in (a) and (b) respectively, for the initial (transpiled) and optimized ESU2 ansatz initialized in the $|\ GHZ\rangle_3$ state. Both the real and imaginary Hinton plots for the COBYLA, NELDER-MEAD, and POWELL optimizers indicates that the final ansatz states were characterized with a loss of quantum purity (thus noisy) as they transformed into completely different mixed states in each optimization pathway.

seen in figure 10, we cannot reliably approximate the ground state eigenvalues [52, 53] of the ^{14}NV-^{13}C system when executing a single and bulky VQC layer as compared to the less noisy QNN inspired multi-layered VQC that has nearly consistent pure ansatz state vectors for each optimizer as we saw in figure 9. However, the errors encountered with the bulky and single layer VQC can possibly be mitigated with techniques like the mid circuit measurement proposed in [51].

At this point, the multi-layered QNN inspired VQC's ability to evaluate the ground state energies and spin states offers valuable quantum dynamical insights into the behavior of NV centers. Our estimates and analysis mainly complement experimental outcomes, demonstrating the potential of our approach to model strongly correlated systems. For example, it has been experimentally established that coherent spin state (CSS) manipulation of a single ^{14}NV center electron spin, surrounded by a nearest neighbor ^{13}C nuclear spin, can be exploited to implement repetitive readout sequences, essentially extending quantum memory for precise measurements [54]. In similar experimental setups, nuclear spins of the ^{14}NV-^{13}C system were polarized and fully controlled through a combination of optical, microwave, and radio frequency fields to showcase the robustness of quantum memory, even in the presence of optical radiation that is required for electronic spin-state readout [54–56]. The coupling of a single NV center with 27 ^{13}C nuclear has also been demonstrated for atomic scale imagery by isolating individual nuclear–nuclear spin interactions [57]. These and many other NV center experimental observations can be supplemented with custom simulations of the QNN-inspired VQC circuit.

In this regard, future work can extend the scope of our designed VQC to encode a 2D Hamiltonian of the ^{14}NV-^{13}C system to model quantum phase transitions, spin squeezing, and spin-lattice relaxation. Advanced dynamical decoupling techniques [58] can also be employed to increase the limits of spin coherence time to that

of spin-lattice relaxation time, effectively minimizing the decoherence effects of surrounding electronic and nuclear spins on the NV-electron spin. Advanced simulations of this type can provide us with quantitative performance metrics of spin qubits to achieve high-fidelity control and consistent quantum information processing protocols in spin-based quantum devices. Techniques for evading barren plateau landscapes can further be explored to enhance the success of gradient-based optimizers on the designed VQC. Therefore, by utilizing the electronic- and nuclear spins of the diamond NV center, which must be well shielded from environmental noise, one can implement a plausible NV-based quantum sensing or quantum computing device [59–63]. This approach can also be applied in modeling other quantum systems in materials science and quantum chemistry. The implications of correctly modeling the behavior of NV center dynamics are far-reaching across quantum technologies. Particularly in quantum computing and information processing, NV centers are potential candidates for qubits, and their precise control of NISQ devices is a critical factor for achieving high fidelities. Future research could extend the scope of our current work to simulate multi-NV center systems with 2D Hamiltonians and employ techniques for mitigating barren plateaus to better assess the performance of gradient-based optimizers on the designed VQC.

3.4. Remarks on QNN inspired VQC architecture

It has to be understood that the quantum circuit implemented in this work is purely a VQC emulating the layered architecture of a quantum feed forward QNN. The QNN inspired structure comes into picture as a consequence of the *Trotterized* propagator which is bifurcated into 7 sub-unitaries (see equation (A14) in Appendix A) of the full time evolution operator. Thus, each sub-unitary represented a parameterized observable that was encoded as a distinct circuit layer of the VQC (resembling a QNN architecture). Hence, by default we had a VQC circuit with 7 layers. Even so, if one wanted to change the number of QNN layers, it would be a plausible approach to systematically vary the default number of QNN layers (L) by either merging or sub-dividing the sub-unitaries to produce fewer or more encoded circuit layers respectively. However, implementation of this technique would require iterations across different numbers of QNN layers (L) for each optimization algorithm, with each L-case having varying numbers of theta parameters. Hence, our future work might as well address the effect of changing the number of circuit layers with respect to theta parameters in each layer.

Since the implemented circuit is not necessarily a QNN in itself (it rather implements a layered architecture inspired from QNNs), we did not dwell much on QNN discussion as we were NOT necessarily training and/or testing the VQC circuit with datasets (rather we aimed at optimally simulating dynamics of the Hamiltonian). However, the exact origins of the VQC circuit layers which emulated the quantum feed-forward QNN architecture were thoroughly discussed in section 2.3.

4. Conclusion

In conclusion, we have successfully designed a QNN-inspired VQC capable of simulating the ground state dynamics of a diamond ^{14}NV center in proximal with a rare ^{13}C isotope. The VQC was structured to mimic a three-layered QNN architecture, comprising *input*, *L hidden*, and *output* layers. This circuit configuration was achieved by decomposing the variational unitary into four distinct variational circuit layers using Trotterization. Three quantum registers for the NV center's electron, ^{14}N, and ^{13}C nuclear spins were created to represent three qubits of the VQC, whose final measurement was stored on three classical registers. These qubits were then initialized using 3-qubit entangling protocols (GHZ_3 and W_3), and the variational circuit of the ESU2 ansatz was optimized with six different initial pseudo-random parameter vectors $\{\vec{\theta}_1, \vec{\theta}_2,\cdots,\vec{\theta}_6\}$, each consisting of 24 theta parameters [i.e. $\vec{\theta}_i(\theta_1, \theta_2,\cdots,\theta_{24})$]. We made use of six classical optimization algorithms, three of which were gradient-based (*BFGS, L-BFGS-B, and ADAM)* and the other three gradient-free *(COBYLA, POWELL, and NELDER-MEAD)* optimizers to minimize the VQC's cost function. Our results show that the gradient-free optimizers excelled at estimating the minimum energy eigenvalues, with the COBYLA algorithm being the quickest. The gradient-based optimizers failed to minimize the cost function due to a barren plateau optimization landscape brought about by the randomly initialized ansatz parameters. Final optimal parameter vectors $\{\vec{\theta}_1^*, \vec{\theta}_2^*,\cdots,\vec{\theta}_6^*\}$ were obtained for each optimization pathway, and their respective ESU2 ansatz states were evaluated to represent our best estimates of the ^{14}NV-^{13}C system's ground state. Thus, our work lays the foundational approach for simulating dynamics in NV center systems using VQCs inspired by QNNs to capture hyperfine effects.

Acknowledgments

This work is supported by the Wits-IBM collaborative project. We further acknowledge funding from the CSIR-NLC, NRF (SA), VRC (Wits) and DSI-SAQTi for supporting our research.

Data availability statement

All data that support the findings of this study are included within the article (and any supplementary files).

Appendix A. Detailed derivation of equations (1)—(16)

The time evolution of the ^{14}NV-^{13}C system can be described using the Schrödinger's time-dependent equation as follows (section 3.6.1 in [33]):

$$i\hbar\frac{\partial}{\partial t}\mid\psi(t_0)\rangle = \hat{H}_{NV}\mid\psi(t_0)\rangle \tag{A1}$$

Then, the time evolution unitary operator (propagator) $\hat{U}(t,\ t_0)$ operating on the initial state described in equation (A2) from the reference time t_0 to some later time t that corresponds to the final state ($\mid\psi(t)\rangle$):

$$i\hbar\frac{\partial}{\partial t}[\hat{U}(t,\ t_0)\mid\psi(t_0)\rangle] = \hat{H}_{NV}[\hat{U}(t,\ t_0)\mid\psi(t_0)\rangle] = \hat{H}_{NV}\mid\psi(t)\rangle \text{ for } t > t_0 \tag{A2}$$

We now try to re-arrange the first part of equation (A2) to get the first-order differential equation:

$$\frac{\partial}{\partial t}[\hat{U}(t,\ t_0)\mid\psi(t_0)\rangle] = -\frac{i}{\hbar}\hat{H}_{NV}[\hat{U}(t,\ t_0)\mid\psi(t_0)\rangle] \tag{A3}$$

$$\frac{\partial}{\partial t}\hat{U}(t,\ t_0) = -\frac{i}{\hbar}\hat{H}_{NV}\hat{U}(t,\ t_0) \tag{A4}$$

Solving for $\hat{U}(t,\ t_0)$ by integrating equation (A4), we get:

$$\begin{aligned}
\tfrac{\partial}{\partial t}\hat{U}(t,\ t_0) &= -\tfrac{i}{\hbar}\hat{H}_{NV}\hat{U}(t,\ t_0)\\
\tfrac{d\hat{U}(t,\ t_0)}{\hat{U}(t,\ \ t_0)} &= -\tfrac{i}{\hbar}\hat{H}_{NV}\,dt\\
\int\left(\tfrac{d\hat{U}(t,\ \ t_0)}{\hat{U}(t,\ \ t_0)}\right) &= -\tfrac{i}{\hbar}\hat{H}_{NV}\int_{t_0}^{t}dt\\
\ln[\hat{U}(t,\ t_0)] &= -\tfrac{i}{\hbar}\hat{H}_{NV}(t-t_0)\\
\therefore\ \hat{U}(t,\ t_0) &= e^{-\left[\frac{i}{\hbar}\hat{H}_{NV}(t-t_0)\right]}
\end{aligned} \tag{A5}$$

Thus, we can re-write the last part of equation (A3) in terms of the value of $\hat{U}(t,\ t_0)$ is defined in equation (A5) to express the entire evolution from the initial ^{14}NV-^{13}C quantum state:

$$\mid\psi(t)\rangle = e^{-\left[\frac{i}{\hbar}\hat{H}_{NV}(t-t_0)\right]}\mid\psi(t_0)\rangle \tag{A6}$$

If we start from an arbitrary point in time and define $t_0 = 0$ and then take the reduced Plank's constant $\hbar = 1$, equation (A6) reduces to:

$$\mid\psi(t)\rangle = e^{-i\hat{H}t}\mid\psi(0)\rangle \tag{A7}$$

where $\mid\psi(0)\rangle$ is the initial state of the ^{14}NV-^{13}C system and $\hat{U}(t) = e^{-i\hat{H}_{NV}t}$ is the time evolution operator representing a finite (or discrete) time translation. Since we know the contributing terms of the ^{14}NV-^{13}C Hamiltonian, we can also re-write the time evolution operator as follows:

$$(t) = e^{-i\hat{H}_{NV}t} = e^{-i[\Delta S_z^2 + P(I_z^{(N)})^2 + \mathbf{B}\cdot(g\mu_B\mathbf{S} - \gamma_N\mathbf{I}^{(N)} - \gamma_C\mathbf{I}^{(C)}) + \mathbf{S}\cdot(\mathbf{A}_N\cdot\mathbf{I}^{(N)} + \mathbf{A}_C\cdot\mathbf{I}^{(C)})]t} \tag{A8}$$

$$\hat{U}(t) = e^{-i(\Delta S_z^2)t}.e^{-i[P(I_z^{(N)})^2]t}.e^{-i[\mathbf{B}\cdot(g\mu_B\mathbf{S})]t}.e^{i[\mathbf{B}\cdot(\gamma_N\mathbf{I}^{(N)})]t}.e^{i[\mathbf{B}\cdot(\gamma\mathbf{I})]t}.e^{-i[\mathbf{S}\cdot(\mathbf{A}_N\cdot\mathbf{I}^{(N)})]t}.e^{-i[\mathbf{S}\cdot(\mathbf{A}\cdot\mathbf{I})]t} \tag{A9}$$

$$\hat{U}(t) = e^{-i\hat{H}_1 t}e^{-i\hat{H}_2 t}e^{-i\hat{H}_3 t}e^{-i\hat{H}_4 t}e^{-i\hat{H}_5 t}e^{-i\hat{H}_6 t}e^{-i\hat{H}_7 t} = e^{-i(\sum_j \hat{H}_j)t} \tag{A10}$$

where:

- $\hat{U}_\Delta(t) = e^{-i(\Delta S_z^2)t} = e^{-i\hat{H}_1 t}$ is the *Zero-field splitting operator* of the ^{14}NV center electron spin (S_z);
- $\hat{U}_P(t) = e^{-i[P(I_z^{(N)})^2]t} = e^{-i\hat{H}_2 t}$ is the *Quadrupole interaction operator* of the ^{14}N nuclear spin ($I_z^{(N)}$);

- $\hat{U}_{\mu_B}(t) = e^{-i[\mathbf{B}\cdot(g\mu_B\mathbf{S})]t} = e^{-i\hat{H}_3 t}$ is the *Zeeman interaction operator* of the electron spin (**S**);
- $\hat{U}_{\gamma_N}(t) = e^{i[\mathbf{B}\cdot(\gamma_N\mathbf{I}^{(N)})]t} = e^{-i\hat{H}_4 t}$ is the *Zeeman interaction operator* of the ^{14}N nuclear spin ($\mathbf{I}^{(N)}$);
- $\hat{U}_{\gamma_C}(t) = e^{i[\mathbf{B}\cdot(\gamma_C\mathbf{I}^{(C)})]t} = e^{-i\hat{H}_5 t}$ is the *Zeeman interaction operator* of the ^{13}C nuclear spin ($\mathbf{I}^{(C)}$);
- $\hat{U}_{\mathbf{A}_N}(t) = e^{-i[\mathbf{S}\cdot(\mathbf{A}_N\cdot\mathbf{I}^{(N)})]t} = e^{-i\hat{H}_6 t}$ is the *Anisotropic hyperfine interaction operator* between the ^{14}NV electron spin (**S**) and the ^{14}N nuclear spin ($\mathbf{I}^{(N)}$);
- $\hat{U}_{\mathbf{A}_C}(t) = e^{-i[\mathbf{S}\cdot(\mathbf{A}_C\cdot\mathbf{I}^{(C)})]t} = e^{-i\hat{H}_7 t}$ is the *Anisotropic hyperfine interaction operator* between the NV electron spin (**S**) and the ^{13}C nuclear spin ($\mathbf{I}^{(C)}$); and
- $\hat{H}_{NV} = \sum_j \hat{H}_j = \hat{H}_1 + \hat{H}_2 + \hat{H}_3 + \hat{H}_4 + \hat{H}_5 + \hat{H}_6 + \hat{H}_7$ is the combined effect of Hamiltonian terms

Thus, equation (A10) can be condensed using the above notation to obtain:

$$\hat{U}(t) = \hat{U}_\Delta(t)\hat{U}_P(t)\hat{U}_{\mu_B}(t)\hat{U}_{\gamma_N}(t)\hat{U}_{\gamma_C}(t)\hat{U}_{\mathbf{A_N}}(t)\hat{U}_{\mathbf{A_C}}(t) \tag{A11}$$

To encode the ^{14}NV-^{13}C Hamiltonian, $\hat{H}_{NV} = \sum_j \hat{H}_j$, we approximated a small-time step δt of the time evolution operator $\hat{U}(t)$ using the first-order *Trotter-Suzuki* decomposition as shown below:

$$\hat{U}(\delta t) = e^{-i\hat{H}_{NV}\delta t} \approx \prod_j e^{-i\hat{H}_{NV\,j}\delta t} \tag{A12}$$

$$\Rightarrow \quad e^{-i\hat{H}_{NV}\delta t} \approx e^{-i\hat{H}_1\delta t}e^{-i\hat{H}_2\delta t}e^{-i\hat{H}_3\delta t}e^{-i\hat{H}_4\delta t}e^{-i\hat{H}_5\delta t}e^{-i\hat{H}_6\delta t}e^{-i\hat{H}_7\delta t}$$

$$= e^{-i(\sum_j \hat{H}_j)\delta t} \tag{A13}$$

$$\Rightarrow \quad \hat{U}(\delta t) \approx e^{-i\hat{H}_{NV}\delta t} \approx \hat{U}_1 \quad \hat{U}_2 \quad \hat{U}_3 \quad \hat{U}_4 \quad \hat{U}_5 \quad \hat{U}_6 \quad \hat{U}_7 \tag{A14}$$

where $\hat{U}_1$, $\hat{U}_2$, $\hat{U}_3$, $\hat{U}_4$, $\hat{U}_5$, $\hat{U}_6$, and $\hat{U}_7$ are unitary operators defined by:

- $\hat{U}_1 = \hat{U}_\Delta(\delta t) \approx e^{-i(\Delta S_z^2)\delta t}$
- $\hat{U}_2 = \hat{U}_P(\delta t) \approx e^{-i[P(I_z^{(N)})^2]\delta t}$
- $\hat{U}_3 = \hat{U}_{\mu_B}(\delta t) \approx e^{-i[\mathbf{B}\cdot(g\mu_B\mathbf{S})]\delta t}$
- $\hat{U}_4 = \hat{U}_{\gamma_N}(\delta t) \approx e^{i[\mathbf{B}\cdot(\gamma_N\mathbf{I}^{(N)})]\delta t}$
- $\hat{U}_5 = \hat{U}_{\gamma_C}(\delta t) \approx e^{i[\mathbf{B}\cdot(\gamma_C\mathbf{I}^{(C)})]\delta t}$
- $\hat{U}_6 \approx e^{-i[\mathbf{S}\cdot(\mathbf{A}_N\cdot\mathbf{I}^{(N)})]\delta t}$
- $\hat{U}_7 \approx e^{-i[\mathbf{S}\cdot(\mathbf{A}_C\cdot\mathbf{I}^{(C)})]\delta t}$

Taking t to be the complete evolution time, then there will be a total of $n = \frac{t}{\delta t}$ *Trotter* steps to achieve complete quantum state propagation from the initial state $|\psi(0)\rangle$ to the final state $|\psi(t)\rangle$. Therefore, we can express the *Trotterized* full-state propagator $\hat{U}(t)$ as:

$$\therefore \hat{U}(t) \approx e^{(-i\hat{H}\delta t)n} \tag{A15}$$

To affect the Hamiltonian encoding, we consider the magnetic field $\boldsymbol{B}$ to be directed along the $z-axis$ (such that $\boldsymbol{B} \equiv B_z$). Thus, we further apply the Bravyi-Kitaev Transformation (BKT) [35] to map terms of the *Trotterised propagator* to their approximated qubit operators [26, 27]. The BKT's quantum gate encoding is implemented as shown in equations (A16–A22) by transforming the electron and nuclear spin operators S_z, $I_z^{(N)}$, $I_z^{(C)}$ to qubit operators $Q_z = \frac{1}{2}Z_i = \frac{1}{2}I_i$, where i is the corresponding qubit index.

$$\hat{U}_\Delta(\delta t) = e^{-i(\Delta S_z^2)\delta t} \approx e^{-i(\Delta Q_z^2)\delta t} \approx e^{-i\left(\frac{\Delta}{4}\right)I_e\delta t}$$

$$\equiv P_{(e)}\left(\frac{\Delta}{2}\delta t\right) \approx P_{(e)}(\theta_\Delta) \Rightarrow \left[S_z^2 \approx \left(\frac{1}{2}z_e\right)^2 = \frac{1}{4}I_e\right] \tag{A16}$$

$$\hat{U}_P(\delta t) = e^{-i[P(I_z^{(N)})^2]\delta t} \approx e^{-i[P(Q_z^{(N)})^2]\delta t} \approx e^{-i\left(\frac{P}{4}\right)I_N\delta t}$$

$$\equiv P_{(N)}\left(\frac{P}{2}\delta t\right) \approx P_{(N)}(\theta_P) \Rightarrow \left[(I_z^{(N)})^2 \approx \left(\frac{1}{2}z_N\right)^2 = \frac{1}{4}I_N\right] \tag{A17}$$

$$\hat{U}_{\mu_B}(\delta t) = e^{-i[\mathbf{B}\cdot(g\mu_B\mathbf{S})]\delta t} \approx e^{-i[(B_z\cdot Q_z)g\mu_B]\delta t} \approx e^{-i\left(\frac{g\mu_B B_z}{2}\right)Z_e\delta t}$$

$$\equiv R_{Z_e}(g\mu_B B_z\delta t) \approx R_{z_e}(\theta_{\mu_B}) \Rightarrow \left[S \approx \left(\frac{1}{2}z_e\right) = \frac{1}{2}Z_e\right] \tag{A18}$$

$$\hat{U}_{\gamma_N}(\delta t) = e^{i[\mathbf{B}\cdot(\gamma_N\mathbf{I}^{(N)})]\delta t} \approx e^{i[(B_z\cdot Q_z^{(N)})\gamma_N]\delta t} \approx e^{i\left(\frac{\gamma_N B_z}{2}\right)Z_N\delta t}$$

$$\equiv R_{Z_N}(-\gamma_N B_z\delta t) \approx R_{z_N}(\theta_{\gamma_N}) \Rightarrow \left[I_z^{(N)} \approx \frac{1}{2}z_N = \frac{1}{2}Z_N\right] \tag{A19}$$

$$\hat{U}_{\gamma_C}(\delta t) = e^{i[\mathbf{B}\cdot(\gamma_C\mathbf{I}^{(C)})]\delta t} \approx e^{i[(B_z\cdot I_z^{(C)})\gamma_C]\delta t} \approx e^{i(\frac{\gamma B_z}{2})Z_C\delta t} \equiv R_{Z_C}(-\gamma B_z\delta t) \approx R_{Z_C}(\theta_{\gamma_C})\left[I_z^{(C)} \approx \frac{1}{2}z_N = \frac{1}{2}Z_N\right] \tag{A20}$$

$$\hat{U}_{\mathbf{A}_N}(\delta t) = e^{-i[\mathbf{S}\cdot(\mathbf{A}_N\cdot\mathbf{I}^{(N)})]\delta t} \approx \prod_{j\langle x,y,z\rangle} e^{-i(S_j\cdot A_{Nj,j}\cdot I_j^{(N)})\delta t}$$
$$\approx e^{-i\left[\left(\frac{A_{Nxx}}{4}\right)X_eX_N+\left(\frac{A_{Nyy}}{4}\right)Y_eY_N+\left(\frac{A_{Nzz}}{4}\right)Z_eZ_N\right]\delta t} \equiv \prod_{j\langle x,y,z\rangle} R_{j_ej_N}\left(\frac{A_{Njj}}{2}\right) \tag{A21}$$

$$\hat{U}_{\mathbf{A}_C}(\delta t) = e^{-i[\mathbf{S}\cdot(\mathbf{A}_C\cdot\mathbf{I}^{(C)})]\delta t} \approx \prod_{j\langle x,y,z\rangle} e^{-i(S_j\cdot A_{Cj,j}\cdot I_j^{(C)})\delta t}$$
$$\approx e^{-i\left[\left(\frac{A_{Cxx}}{4}\right)X_eX_C+\left(\frac{A_{Cyy}}{4}\right)Y_eY_C+\left(\frac{A_{Czz}}{4}\right)Z_eZ_C\right]\delta t} \equiv \prod_{j\langle x,y,z\rangle} R_{j_ej_C}\left(\frac{A_{Cjj}}{2}\right) \tag{A22}$$

where $\boldsymbol{j} \in \{x, y, z\}$.

Since $\hat{H}_{NV} = \sum_j \hat{H}_j = \hat{H}_1 + \hat{H}_2 + \hat{H}_3 + \hat{H}_4 + \hat{H}_5 + \hat{H}_6 + \hat{H}_7$, the Hamiltonian can then be encoded as an observable of the VQC with quantum gates defined in equations (A16–A22).

$$\hat{\boldsymbol{H}}_{\boldsymbol{NV}} = \left(\frac{\boldsymbol{\Delta}}{4}\right)\boldsymbol{I}_e + \left(\frac{\boldsymbol{P}}{4}\right)\boldsymbol{I}_N + \left(\frac{g\mu_B\boldsymbol{B}_z}{2}\right)\boldsymbol{Z}_e$$
$$-\left(\frac{\gamma_N\boldsymbol{B}_z}{2}\right)\boldsymbol{Z}_N - \left(\frac{\gamma\boldsymbol{B}_z}{2}\right)\mathbf{Z}_C + \left[\left(\frac{\mathbf{A}_{Nxx}}{4}\right)\mathbf{X}_e\mathbf{X}_N + \left(\frac{\mathbf{A}_{Nyy}}{4}\right)\mathbf{Y}_e\mathbf{Y}_N + \left(\frac{\mathbf{A}_{Nzz}}{4}\right)\mathbf{Z}_e\mathbf{Z}_N\right]$$
$$+\left[\left(\frac{\boldsymbol{A}_{Cxx}}{4}\right)\boldsymbol{X}_e\boldsymbol{X}_C + \left(\frac{\boldsymbol{A}_{Cyy}}{4}\right)\boldsymbol{Y}_e\boldsymbol{Y}_C + \left(\frac{\boldsymbol{A}_{Czz}}{4}\right)\boldsymbol{Z}_e\boldsymbol{Z}_N\right] \tag{A23}$$

Appendix B. VQC observables and parameters

B.1. VQC hamiltonian encoding

Detailed quantum gate encoding of the Hamiltonian into the VQC's observable in equation (A23) is shown in table B1.

B.2. VQC circuit parameters

Table B2 shows the VQC parameters defined based on the couplings and coefficients determined theoretically and/or experimentally for ^{14}NV-^{13}C systems [21, 29–32].

Table B1. Quantum logic gate implementation of the VQC observable in equation (A23).

Observable	Equivalent gates	Qubits involved	Sparse pauli operators ($Q_C Q_N Q_e$)
$\left(\frac{\Delta}{4}\right)I_e$	$P_{(e)}(\theta_\Delta)$	Electron spin qubit (Global Phase)	III
$\left(\frac{P}{4}\right)I_N$	$P_{(N)}(\theta_P)$	^{14}N nuclear spin qubits (Global Phase)	III
$\left(\frac{g\mu_B B_z}{2}\right)Z_e$	$R_{Ze}(\theta_{\mu_{Bz}})$	Electron spin qubit (Single-Qubit Gate)	IIZ
$\left(\frac{\gamma_N B_z}{2}\right)Z_N$	$R_{zN}(\theta_{\gamma_N})$	^{14}N nuclear spin qubit (Single-Qubit Gate)	IZI
$\left(\frac{\gamma B_z}{2}\right)Z_C$	$R_{Z_C}(\theta_{\gamma_C})$	^{13}C nuclear spin qubit (Single-Qubit Gate)	ZII
$\left(\frac{A_{Nxx}}{4}\right)X_e X_N$	$R_{X_e X_N}(\theta_{ANxx})$	Electron and ^{14}N nuclear spin qubits (2-Qubit Gates)	IXX
$\left(\frac{A_{Nyy}}{4}\right)Y_e Y_N$	$R_{X_e X_N}(\theta_{ANyy})$	Electron and ^{14}N nuclear spin qubits (2-Qubit Gates)	IYY
$\left(\frac{A_{Nzz}}{4}\right)Z_e Z_N$	$R_{X_e X_N}(\theta_{ANzz})$	Electron and ^{14}N nuclear spin qubits (2-Qubit Gates)	IZZ
$\left(\frac{A_{Cxx}}{4}\right)X_e X_C$	$R_{X_e X_C}(\theta_{ACxx})$	Electron and ^{13}C nuclear spin qubits (2-Qubit Gates)	XIX
$\left(\frac{A_{Cyy}}{4}\right)Y_e Y_C$	$R_{X_e X_C}(\theta_{ACyy})$	Electron and ^{13}C nuclear spin qubits (2-Qubit Gates)	YIY
$\left(\frac{A_{Czz}}{4}\right)Z_e Z_N$	$R_{X_e X_C}(\theta_{ACzz})$	Electron and ^{13}C nuclear spin qubits (2-Qubit Gates)	ZIZ

Table B2. List of VQC circuit parameters and their definitions.

Circuit parameters	Parameter definition
δt	$\delta t = \frac{Evolution\ Time(t)}{Num.\ Trotter\ Steps(n)} = 0.002$ (with time $t = 1$, we have $n = 500$)
B_j	$B_j = B_z = \boldsymbol{B} = 1T$ (Magnetic field along the z-direction)
$\theta_\Delta = 2\Delta\delta t$	$\Delta \approx 2.87GHz$
$\theta_{P_l} = 2P_l\delta t$	$P_1 = P_2 = P_3 = P = -5MHz$
$\theta_{\mu_{Bj}} = g\mu_B B_j \delta t$	$g = g_\parallel = 2.0029$ and $g_\perp = 2.0031$ $\mu_B \approx 5.788 \times 10^{-5} eV/T$
$\theta_{\gamma_{Nj}} = -\gamma_N B_j \delta t$	$\theta_{\gamma_{Nj}} = \theta_{\gamma_{Nz}}$ and $\gamma_N = 3.077$ MHz T $-$ (2π space)
$\theta_{\gamma_{c13j}} = -\gamma_{c13} B_j \delta t$	$\theta_{\gamma_{c13j}} = \theta_{\gamma_{c13z}}$ and $\gamma_{c13} = 10.705$MHz/T (2π space)
$\theta_{A_{Nj}} = A_{Nj}\delta t$	$A_{Nx} = A_{Ny} = \boldsymbol{A}_{N\perp} = -2.70MHz$ (^{14}N Anisotropic Hyperfine Interaction Tensor) $A_{Nz} = \boldsymbol{A}_{N\parallel} = -2.16MHz$ (^{14}N Isotropic Hyperfine Interaction Tensor)
$\theta_{A_{c13j}} = A_{c13j}\delta t$	$A_{c13x} = A_{c13y} = \boldsymbol{A}_\perp = 120.3MHz$ (^{13}C Anisotropic Hyperfine Interaction Tensor) $A_{c13z} = \boldsymbol{A}_\parallel = 199.7MHz$ (^{13}C Isotropic Hyperfine Interaction Tensor)

Appendix C. Data repository (source code and files)

The following google drive link redirects to a cloud folder where the IMB's Qiskit source code (implemented in Python) and the data files (csv and json) containing optimization results for the six optimizers used in this study are stored.

https://drive.google.com/drive/folders/1YqCJgUM0V_XWTBLG8oBVMOvYB2ga322G?usp=drive_link

Conflict of interest

The authors declare no conflict of interest.

Ethical statement

This study does NOT in any way involve live subjects (human or animal).

ORCID iDs

Chisomo Daka https://orcid.org/0000-0001-9465-5507
Somnath Bhattacharyya https://orcid.org/0000-0002-8744-2527

References

[1] Feynman R P 1982 *Int. J. Theor. Phys.* **21** 467–88
[2] Muller R P and Blume-Kohout R 2015 *ACS Nano.* **9** 7738–41
[3] Daley A J *et al* 2022 *Nature* **607** 667–76
[4] Georgescu I M, Ashhab S and Nori F 2014 *Rev. Mod. Phys.* **86** 153
[5] Arute F *et al* 2019 *Nature* **574** 505–10
[6] Bharti K 2022 *Rev. Mod. Phys.* **94** 015004
[7] Shor P W 1997 *SIAM J. Comput.* **26** 1484–509
[8] Wang K *et al* 2022 *npj Quantum Inf.* **8** 52
[9] Cerezo M *et al* 2021 *Nat. Rev. Phys.* **3** 625–44
[10] Kandala A *et al* 2017 *Nature* **549** 242–6
[11] Sapova M D and Fedorov A K 2022 *Commun. Phys.* **5** 199
[12] Beer K *et al* 2020 *Nat. Commun.* **11** 808
[13] Acosta V and Hemmer P 2013 *MRS Bull.* **38** 127–30
[14] Maurer P C *et al* 2012 *Science* **336** 1283–6
[15] Maze J *et al* 2008 *Nature* **455** 644–7
[16] Balasubramanian G *et al* 2008 *Nature* **455** 648–51
[17] Thiering G and Gali A 2020 *Semicond. Semimet.* **103** 1–36
[18] Ríos J M 2010 Quantum manipulation of nitrogen-vacancy centers in diamond: From basic properties to applications *Ph.D Theses* Havard University
[19] Smeltzer B *et al* 2011 *New J. Phys.* **13** 025021
[20] Bhattacharyya S 2024 *Carbon Superstructures: From Quantum Transport to Quantum Computation* 1st ed. (CRC Press)
[21] Mazhandu F *et al* 2019 *Appl. Phys. Lett.* **115** 233501
[22] Bhattacharyya S and Bhattacharyya S 2022 *Entropy* **24** 1593
[23] Mahony D and Bhattacharyya S 2021 *Appl. Phys. Lett.* **118** 20404
[24] Lee C K, Patil P, Zhang S and Hsieh C Y 2021 *Phys. Rev. Res.* **3** 023095
[25] Li Z, Xiao T, Deng X, Zeng G and Li W 2024 *Mathematics* **12** 1627
[26] Grant E, Wossnig L, Ostaszewski M and Benedetti M 2019 *Quantum* **3** 214
[27] McClean J R *et al* 2018 *Nat. Commun.* **9** 4812
[28] Ge X, Wu R B and Rabitz H 2022 *Annu. Rev. Control* **54** 314–23
[29] Felton S *et al* 2009 *Phys. Rev.* B **79** 075203
[30] Smeltzer B *et al* 2009 *Phys. Rev.* A **80** 050302 (R)
[31] Steiner M *et al* 2010 *Phys. Rev.* B **81** 035205
[32] Goldblatt R M *et al* 2022 *Phys. Rev.* B **105** L020405
[33] Zettili N 2009 *Quantum Mechanics: Concepts and Applications* 2nd Ed. (Wiley)
[34] Kim Y *et al* 2023 *Nature* **618** 500–5
[35] Bravyi S B and Kitaev A Y 2002 *Ann. Phys.* **298** 210–26
[36] Seeley J T, Richard M J and Love P J 2012 *J. Chem. Phys.* **137** 224109
[37] Song J, Lu B, Liu L and Wang C 2023 *Electronics* **12** 2430
[38] Jameson A 1995 *Gradient Based Optimization Methods MAE Technical Report No* **2057** 1 http://aero-comlab.stanford.edu/Papers/jameson.gbom.pdf
[39] Qian Y, Du Y and Tao D 2024 *Quantum Mach. Intell.* **6** 1
[40] Cruz D *et al* 2019 *Adv. Quantum Technol.* **2** 5–6
[41] Qiskit Community 2021 *Qiskit Community Tutorials: W state in multi-qubit systems GitHub.* https://github.com/qiskit-community/qiskit-community-tutorials/blob/master/awards/teach_me_qiskit_2018/w_state/W%20State%201%20-%20Multi-Qubit%20Systems.ipynb Retrieved on 11th June, 2024.
[42] TwoLocal 2024 *IBM Quantum Documentation (n.d)* https://docs.quantum.ibm.com/api/qiskit/qiskit.circuit.library.TwoLocal
[43] EfficientSU2 2024 *IBM Quantum Documentation (n.d)* https://docs.quantum.ibm.com/api/qiskit/qiskit.circuit.library.EfficientSU2
[44] BackendEstimatorV2 2024 *IBM Quantum Documentation (n.d.)* https://docs.quantum.ibm.com/api/qiskit/qiskit.primitives.BackendEstimatorV2
[45] System Information 2024 *IBM Quantum Documentation (n.d.-b.).* https://docs.quantum.ibm.com/guides/qpu-information#system-configuration-values Retrieved on 13th June,
[46] Sack S H *et al* 2022 *PRX Quantum* **3** 020365
[47] Friedrich L and Maziero J 2022 *Phys. Rev.* A **106** 042433
[48] Broers L and Mathey L 2024 *Phys. Rev. Res.* **6** 013076
[49] Goyeneche D and Życzkowski K 2014 *Phys. Rev.* A **90** 022316
[50] Zhu C, Xu F and Pei C 2015 *Sci. Rep.* **5** 17449
[51] Botelho L *et al* 2022 *Phys. Rev.* A **105** 022441
[52] LaRose R *et al* 2019 *Quantum Inf* **5** 57
[53] Claudino D *et al* 2020 *Front. Chem.* **8** 606863
[54] Jiang L *et al* 2009 *Science* **326** 267–72
[55] Dutt M *et al* 2007 *Science* **316** 1312–6
[56] Jiang L *et al* 2008 *Phys. Rev. Lett.* **100** 073001
[57] Abobeih M H *et al* 2019 *Nature* **576** 411–5
[58] Abobeih M H *et al* 2018 *Nat. Commun.* **9** 2552
[59] Vallabhapurapu H *et al* 2023 *Phys. Rev.* A **108** 022606
[60] Yang L, Wang H, Yang S and Lu Y 2024 *Mater. Quantum Technol.* **4** 023001
[61] Pezzagna S and Meijer J 2021 *Appl. Phys. Rev.* **8** 011308
[62] Childress L and Hanson R 2013 *MRS Bull.* **38** 134–8
[63] Rembold P *et al* 2020 *AVS Quantum Sci.* **2** 024701